Research Square

Preprints are preliminary reports that have not undergone peer review.
They should not be considered conclusive, used to inform clinical practice,
or referenced by the media as validated information.

Embedded Predictive Control for an Autonomous Waste-Collection Unmanned Surface Vehicle

Chiaka Chibuike David
Fujian Agriculture and Forestry University
Xueyong Chen
xueyongchen@fafu.edu.cn
Fujian Agriculture and Forestry University

Research Article

Keywords: generalized predictive control, PID control, cascade control, waste collection, unmanned surface vehicle, embedded control, genetic programming

Posted Date: November 25th, 2026

DOI: https://doi.org/10.21203/rs.3.rs-11327403/v1

License: This work is licensed under a Creative Commons Attribution 4.0 International License.
Read Full License

Additional Declarations: No competing interests reported.

Embedded Predictive Control for an Autonomous Waste-Collection Unmanned Surface Vehicle

Chiaka Chibuike David[1], Xueyong Chen[1]*

[1] College of Mechanical and Electrical Engineering, Fujian Agriculture and Forestry University, Fuzhou 350001, China; 12331013015@fafu.edu.cn (C.C.D.); *Correspondence: xueyongchen@fafu.edu.cn

ORCID iDs: Chiaka Chibuike David, https://orcid.org/[0009-0009-2313-3125]; Xueyong Chen, https://orcid.org/[0000-0002-4765-4066]

Abstract

Background: Model predictive control (MPC) can compensate for delay and handle constraints in autonomous surface vehicles, but its online computational burden has limited its use on low-power embedded hardware. This paper develops and field-tests a computationally constrained generalized predictive control (GPC)–proportional–integral–derivative (PID) cascade for an autonomous waste-collection unmanned surface vehicle (USV) operating in the Minjiang River, Fuzhou. The architecture separates slow, delay-dominated heading dynamics (outer GPC loop) from fast disturbances (inner PID loop). A conveyor controller uses offline genetic-programming (GP) optimization followed by deterministic online gain scheduling.

Results: Field trials were conducted under wind speeds of 0-8 m/s and flow velocities of 0.3-1.2 m/s. Relative to a conventional PID baseline, the GPC-PID controller reduced mean cross-track error (XTE) from 2.31 to 0.96 m (58.4%, Welch's $t(33.1) = 41.86$, $p < 0.001$, 95% CI of the reduction [1.28, 1.42] m), reduced RMS rudder angle from 8.5° to 3.5° (58.8%), and shortened disturbance settling time from 6.2 to 3.1 s (50.0%). Average navigation power fell from 98 to 71 W (27.5%), and 30-minute mission energy fell from 57.6 to 48.1 Wh (16.5%), while endurance increased from 3.4 to 4.7 h (38.2%). On a 1.8 GHz ARM Cortex-A72 processor, GPC execution

averaged 4.2 ms, with a 95th percentile of 5.8 ms and a worst case of 8.1 ms against a 100 ms deadline; 18 of 180,000 system control cycles missed the deadline by less than 1 ms, due to scheduling jitter, while GPC execution itself never exceeded 8.1 ms. For solid debris under moderate wind, GP-PID collection efficiency was 94.2 ± 4.2% (plastic bottles), 91.5 ± 5.6% (styrofoam), and 89.3 ± 6.4% (natural leaves), versus 87.3 ± 7.0%, 83.1 ± 8.4%, and 81.7 ± 9.6% for fixed-gain PID. Oil films were excluded from field collection trials because detection precision (0.71) and conveyor compatibility were insufficient; no field collection efficiency is reported for liquid pollutants. The oil-film value (52.0%) comes from a controlled simulation and is not a field result.

Conclusions: Predictive control was feasible on low-power embedded hardware when computational constraints were treated as design requirements, but the achievable performance is bounded by perception latency, actuator delay, payload limits, and environmental conditions. The framework can serve as a template for embedded predictive control in resource-constrained environmental robotics, provided that worst-case timing, perception degradation, and failure modes are reported alongside mean performance.

Keywords*:* generalized predictive control; PID control; cascade control; waste collection; unmanned surface vehicle; embedded control; genetic programming

1. Introduction

1.1 Background

Inland and coastal waterways are major conduits and accumulation zones for anthropogenic waste. Estimates indicate that between 1.15 and 2.41 million tonnes of plastic waste enter the ocean annually through riverine systems (Lebreton et al., 2017; Schmidt et al., 2017),

and that more than 1,000 rivers account for approximately 80% of global riverine plastic emissions (Meijer et al., 2021). A substantial fraction of this material remains afloat or is retained in estuaries and freshwater systems (Eriksen et al., 2014; Isobe & Iwasaki, 2022). The Minjiang River in Fuzhou, China, exemplifies this problem: microplastic concentrations in the lower reaches have been reported at 19.90-22.87 particles/L in surface water and 728.17 particles/kg in sediments, with ecological risk classified as very high (Bao et al., 2025).

Conventional remediation relies on manned vessels, which are inefficient in shallow, cluttered water, economically burdensome, and hazardous to personnel. Unmanned surface vehicles (USVs) offer an alternative that can operate continuously without placing personnel at risk (Caccia et al., 2008; Fossen, 2011). However, the transition from passive monitoring to active waste collection introduces tightly coupled control and perception requirements that existing platforms do not fully address.

USV control is complicated by large inertia, significant actuation delay, nonlinearity, and stochastic environmental disturbance. Classical PID controllers remain widely used because of their simplicity and computational efficiency (Åström & Hägglund, 2006), but they are reactive: they respond to past errors and therefore perform poorly in delay-dominated systems. Active disturbance rejection control (ADRC) estimates and compensates for total disturbance and offers improved robustness with modest computation (Han, 2008, 2009; van der Saag et al., 2025), yet it lacks multi-step prediction and remains fundamentally reactive to future trajectory requirements.

Predictive control addresses delay explicitly through multi-step prediction and receding-horizon optimization (Clarke et al., 1987; Normey-Rico & Camacho, 2007). Generalized predictive control (GPC) is applicable to delay-dominated plants because it requires little model-structure detail and admits a closed-form control law for the CARIMA formulation (Clarke et al.,

1987; Clarke & Mohtadi, 1989). However, conventional MPC requires the online solution of a quadratic program whose complexity scales cubically with the control horizon (Wang, 2009; Camacho & Bordons, 2007). Explicit MPC pre-computes the control law offline but incurs exponential memory growth with problem dimension (Bemporad et al., 2002). Recent work has reduced the computational burden through algorithm-hardware co-design: Tiny-MPC achieves millisecond-scale solve times on microcontrollers via ADMM and problem-structure exploitation (Nguyen et al., 2024), and neural-augmented MPC reduces online computation while preserving constraint satisfaction (Alsmeier et al., 2024; Kouvaritakis & Cannon, 2016). Neural-network adaptive controllers and hybrid approaches can perform well but typically require more computation than cost-sensitive environmental robotics platforms provide and often lack formal stability guarantees (Ren et al., 2023; Fan et al., 2019). Recent work on MPC for ships includes parametric dynamic modeling approaches (Wang et al., 2025) and data-driven Gaussian-process MPC (Xu et al., 2023). Reinforcement-learning-based path following has also been validated experimentally (Wang et al., 2023).

Cascade structures separate slow and fast dynamics and are widely used in process control (Skogestad, 2003). Marine applications of cascade and delay-compensated control have been reported for dynamic positioning and autonomous vehicles (Hu et al., 2023; Pedersen et al., 2023; Marques et al., 2020; Li et al., 2024). To our knowledge, a field-tested framework that combines predictive delay compensation with embedded feasibility and adaptive subsystem control for a small waste-collection USV has not been reported.

This paper makes four contributions: (i) A GPC-PID cascade architecture that decouples dual-timescale vessel dynamics and executes within a 100 ms control period on a 1.8 GHz ARM processor, with measured mean, 95th-percentile, and worst-case timing. (ii) A horizon-selection

procedure that balances prediction length against computational load and is checked against the identified 0.35 s effective delay. (iii) A two-layer conveyor controller combining offline GP optimization with deterministic online gain scheduling, with a fixed-gain fallback, tested over a 0.1-2.5 kg payload range. (iv) Field testing in the Minjiang River, including a report of experimental challenges and failure modes, with field and simulation results kept separate.

2. System Design and Architecture

2.1 Overall Architecture

The USV is a cyber-physical system (Lee, 2008) comprising five functional modules: locomotion and power, perception and localization, collection, communication, and main control, coordinated by a central embedded computer. Perception and localization supply state and environmental data to the main control system, which computes locomotion and collection commands and maintains a link to the base station (Figure 1).

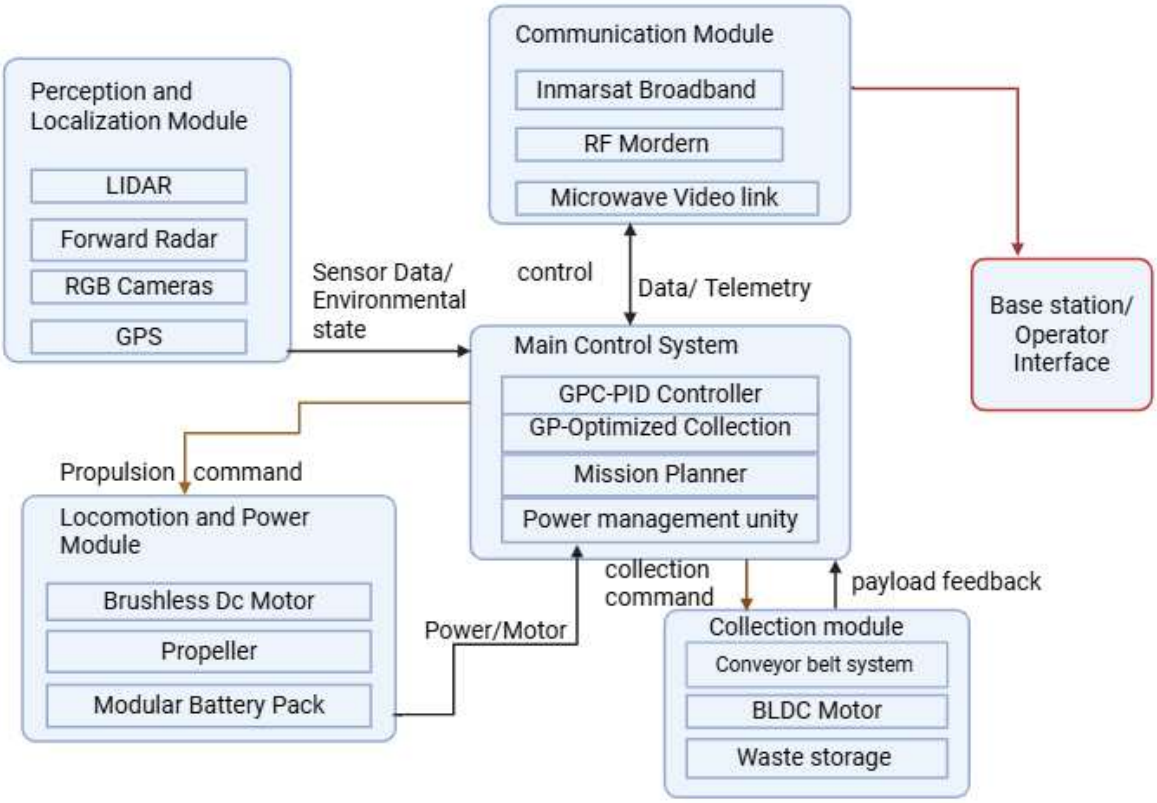


Figure 1. Integrated cyber-physical system architecture of the waste-collection USV.

Perception and localization outputs are fused in the main control system, which issues commands to the locomotion and collection modules; the communication module provides telemetry and supervisory links to the base station.

2.2 Platform and Hull Design

The platform is a catamaran hull fabricated from 304 stainless steel (1.5 mm gauge), selected for strength, durability, and corrosion resistance. The catamaran configuration provides lateral stability for the forward-mounted collection mechanism. The hull is subdivided into watertight compartments filled with polyurethane foam to preserve buoyancy after damage. Platform parameters are listed in Table 1; Figure 2 shows the CAD render and a field photograph.

Table 1. USV Platform Design Parameters

Parameter	Value/unit
Hull length (L)	1.86 m
Beam (B)	0.79 m
Depth (D)	0.42 m
Draft (T)	0.18 m
Freeboard (F)	0.24 m
Hull Material	304 Stainless Steel, 1.5 mm gauge
Total Displacement (Δ)	52.0 kg
Propulsion	Dual BLDC, 3-blade propeller (0.18 m dia.)
Power System	24 V $LiFePO_4$, 480 Wh (20 Ah)
Operational Speed	0.8-1.5 m/s (1.5-3.0 knots)

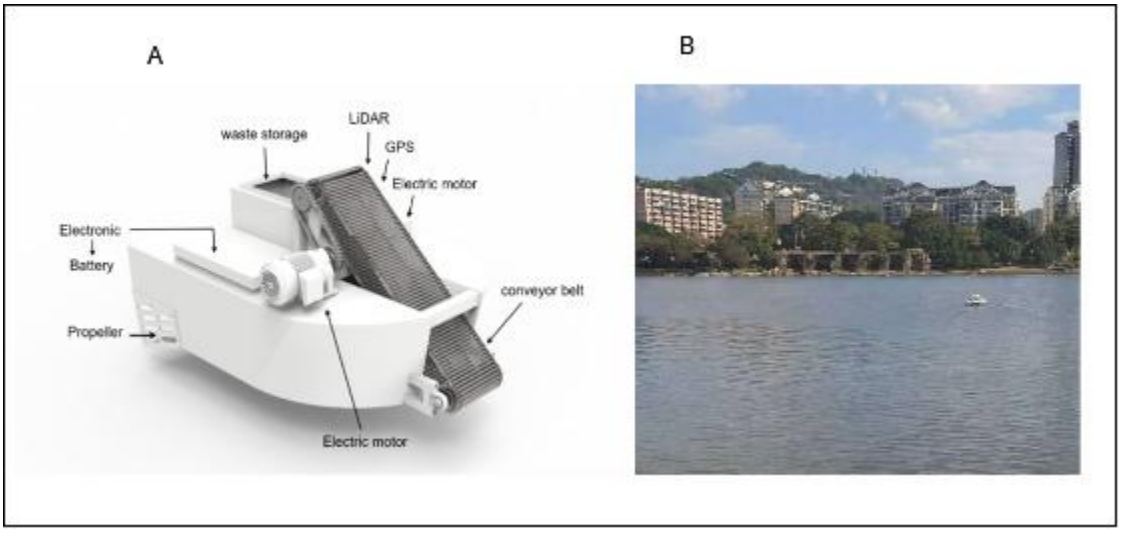


Figure 2. USV platform.

(A) CAD render showing the catamaran hull, forward conveyor, collection bin, LiDAR, GPS, and propulsion units. (B) Field photograph of the assembled vehicle on the Minjiang River.

2.3 Core Functional Modules

2.3.1 Locomotion and Power

Two brushless DC (BLDC) motors drive three-blade propellers through a coupling; a servo-driven rudder provides heading control. The powertrain is powered by a 24 V $LiFePO_4$ battery pack (480 Wh, 20 Ah), giving zero operational emissions and a low acoustic signature. The power management unit (PMU) monitors current and voltage at 10 Hz and allocates power among propulsion, steering, perception, and collection. Nominal endurance exceeds three hours at cruise speed.

2.3.2 Main Control System

The main control system is an embedded industrial computer with a 1.8 GHz quad-core ARM Cortex-A72 processor and 4 GB RAM, running a PREEMPT-RT-patched Linux 5.15 kernel. It executes the GPC and PID loops, the conveyor scheduling routine, path planning, obstacle avoidance, mission logic, and perception fusion. Electronics are housed in a waterproof, vibration-damped, actively cooled enclosure.

2.3.3 Perception and Localization

Localization fuses dual-antenna RTK-GPS, an inertial measurement unit (IMU), and a fiber-optic gyroscope (FOG, OCTANS) through a Kalman filter, providing centimetre-level position and attitude at 100 Hz. Obstacle and waste detection use a 2D LiDAR (Sick TIM series, 270° field of view, up to 25 m, ~1 cm accuracy) Table 2, a forward-looking millimeter-wave radar, and a calibrated stereo camera pair. A convolutional neural network (CNN, MobileNetV3 backbone, 416 × 416 input, quantization-aware training) classifies floating objects. The detection pipeline is: (i) temporal synchronization and spatial registration to the body frame; (ii) Euclidean

clustering and multi-hypothesis tracking; (iii) semantic classification of tracked clusters; and (iv) Bayesian fusion of geometric and semantic evidence into a probabilistic world map (Figure 3; Chang et al., 2021; Abd Alhattab et al., 2025; Zheng et al., 2024; Neves et al., 2023).

Table 2. Sensor specifications.

Sensor	Model	Range	Accuracy	Rate
LiDAR	Sick TIM series	25 m	~1 cm	10 Hz
Radar	Navico 4G	36 nm	±1.5 m	10 Hz
GPS	u-blox ZED-F9P	—	±1 cm (RTK)	10 Hz
IMU	Xsens MTi-30	—	±0.5°	100 Hz
FOG	OCTANS	—	±0.1°	100 Hz
Camera	FLIR Blackfly	—	—	30 Hz

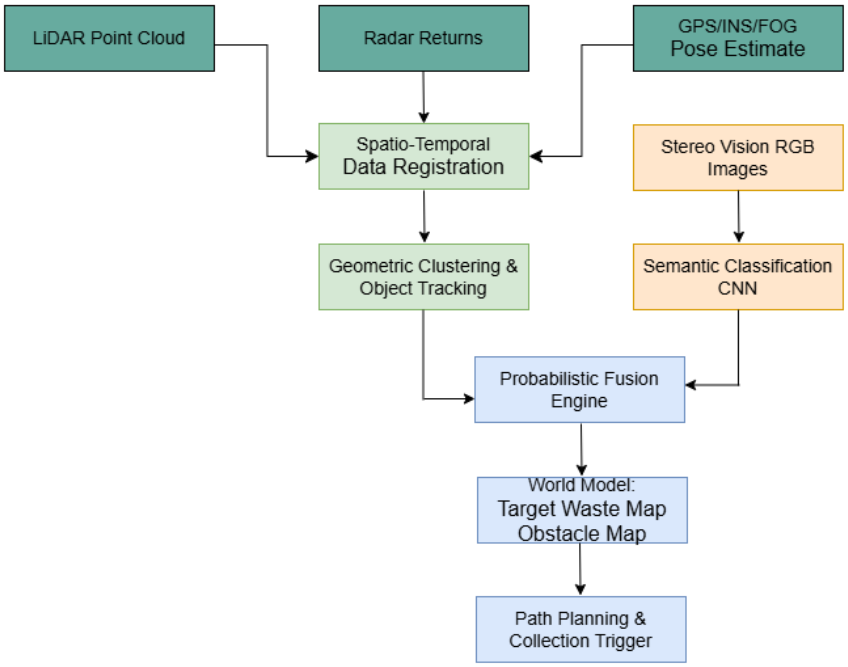


Figure 3. Multi-modal perception and waste-detection pipeline.

LiDAR, radar, and stereo-vision data are registered to the body frame, clustered and tracked, classified by the CNN, and fused probabilistically to produce the world map used by the planner and collection subsystem.

2.3.4 Collection Module

The collection mechanism is a front-mounted conveyor with a low-profile intake ramp, a cleated rubber belt driven by a waterproof BLDC motor through a gearbox, a partitioned collection bin with drainage, and a capacitive fill-level sensor (Figure 4). Belt speed is variable from 0 to 1.5 m/s and is regulated by the conveyor controller described in Section 3.4. The bin volume (15 L) and average debris density limit the tested payload to 0.1-2.5 kg.



Figure 4. Waste-collection mechanism: (1) intake ramp, (2) conveyor belt, (3) BLDC drive motor, (4) collection bin with drainage, and (5) fill-level sensor.

2.3.5 Communication

Communication uses three tiers: an Inmarsat Fleet Broadband link for long-range telemetry and supervision; an RF modem for control and data within approximately 2 km; and a microwave

video link for real-time camera feeds. All critical control and decision-making run onboard; remote supervision is not required for safe operation.

2.4 Control Design Trade-off

Table 3 compares candidate embedded control methods. Conventional MPC handles delay and constraints explicitly but requires online quadratic programming with cubic complexity in the control horizon. Explicit MPC reduces online computation to a lookup but requires memory that grows exponentially with problem dimension. PID and ADRC are computationally light but lack prediction. Neural adaptive controllers offer adaptation at high computational cost and with limited stability guarantees. The proposed GPC–PID cascade occupies the intermediate region: it retains prediction through a closed-form GPC law, offloads high-frequency rejection to a lightweight PID, and is implemented with pre-computed gain matrices.

Table 3. Comparative analysis of embedded control methods for USVs.

Method	**Computational complexity**	**Delay compensation**	**Constraint handling**	**Embedded feasibility**
Conventional MPC	$O(N^3 n_u^3)$	High	Explicit	Low (>50 ms)
Explicit MPC	$O(1)$ lookup	Moderate	Pre-computed	Moderate (memory-intensive)
PID	$O(1)$	None	Implicit (tuning)	High
ADRC	$O(n_u^2)$	Limited	Implicit	Moderate
Neural adaptive	$O(W)$, network size	Moderate	Limited	Low
Proposed GPC–PID	$O(N_u^3 + N_u N_2)$	High	Explicit	High (measured mean 4.2 ms)

3. Control Methodology

3.1 Vessel Dynamics and Identification

System identification was conducted in a calm section of the Minjiang River (flow < 0.2 m/s) at 1.2 m/s. Heading was recorded with the FOG at 100 Hz. The steering servo (HJ S3315D, 15 kg·cm) was excited with 10° step inputs and its response approximated by a first-order lag:

$$G_{act}(s) = \frac{1}{0.12s + 1}$$

where 0.12 s corresponds to the manufacturer-specified servo response (0.12 s/60° at 6.0 V). The yaw response to a 10° rudder step was fitted using the prediction-error method (Ljung, 1999; Nomoto, 1982; Nakatani et al., 2011). The identified Nomoto parameters are given in Table 4; the model achieved a 92% fit on validation data.

Table 4. Identified yaw-dynamics parameters.

Parameter	Value	Interpretation	95% Confidence Interval
K	$0.85\ s^{-1}$	Steady turning rate gain	$[0.78, 0.92]$
T	0.42 s	Yaw rate time constant	$[0.38, 0.46]$
fit	92%	Validation data RMSE	—

3.2 Time-Delay Analysis

The total effective delay was measured component by component (Table 5). The aggregate τ = 0.35 s is the value used for horizon selection and for interpreting the navigation results.

Table 5. Composition of the total effective delay $\tau = 0.35$ s.

component	Delay (ms)	Source
Actuator mechanical	120	Servo response (T_{act})
Serial communication	85	RS-485 @ 115200 baud + packet overhead
Sensor filtering	95	FOG low-pass filter (10 Hz cutoff)
Control loop jitter	50	Worst-case scheduling delay
Total	350	$\tau = 0.35$ s

3.3 GPC–PID Cascade Controller

The cascade separates long-horizon planning from high-frequency rejection. The outer GPC computes a desired rudder angle from the reference trajectory; the inner PID tracks that command at 100 Hz and rejects fast disturbances. The geometric definition of cross-track error and heading correction is shown in Figure 5.

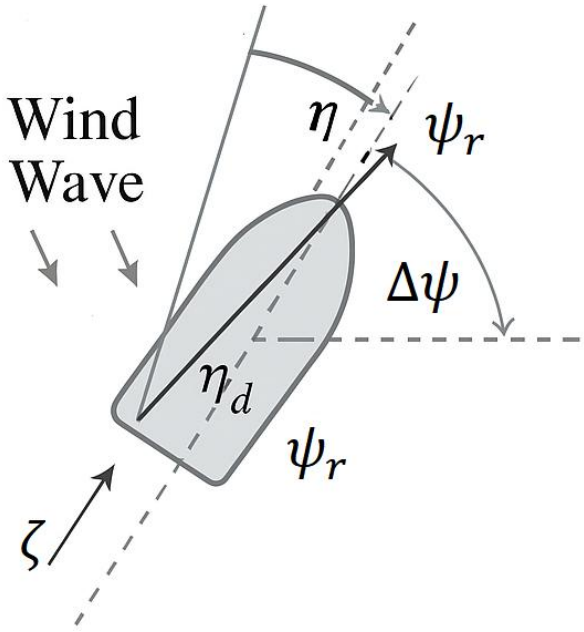


Figure 5. Geometric deviation of the USV from the desired track.

Cross-track error η, reference heading ψ_r, and heading correction $\Delta\psi$

3.3.1 Outer Loop: Generalized Predictive Control

The cascade structure separates the control tasks: an outer loop using Generalized Predictive Control (GPC) handles long-horizon planning and delay compensation, while an inner loop with a fast PID controller rejects high-frequency disturbances (Figure 6).

The GPC uses a CARIMA model (Clarke et al., 1987):

$$A(z^{-1})\psi(t) = B(z^{-1})\delta(t-1) + \frac{\xi(t)}{\Delta},$$

with $\Delta = 1 - z^{-1}$. Zero-order-hold discretization of the identified Nomoto model at $T_s = 0.1$ s (10 Hz; Franklin et al., 1998) gives

$A(z^{-1}) = 1 - 1.881z^{-1} + 0.883z^{-2}$,

$B(z^{-1}) = 0.0059z^{-1} + 0.0054z^{-2}$.

A first-order reference filter generates the smoothed setpoint:

$$\psi_{ref}(t+j) = \alpha\psi_{ref}(t+j-1) + (1-\alpha)\psi_{desired}(t+j)$$

with α = 0.95. The cost function is (Yusof & Omatu, 1991; Scattolini & Bittanti, 1990):

$$J = \sum_{j=N_1}^{N_2} \left[\psi_{ref}(t+j) - \hat{\psi}(t+j \mid t)\right]^2 + \lambda \sum_{j=1}^{N_2} [\Delta u(t+j-1)]^2$$

with $N_1 = 1$, $N_2 = 10$, $N_u = 3$, and $\lambda = 0.1$. The 1.0 s prediction horizon covers about three times the 0.35 s effective delay. The control law is

$$\Delta\delta = (G^T G + \lambda I)^{-1} G^T (w - f)$$

where G contains the step-response coefficients, w the future references, and f the free response. G is pre-computed offline; online computation is matrix–vector multiplication only. The condition number of $(G^T G + \lambda I)$ remained below 10^3 across operating conditions (Golub & Van Loan, 1996).

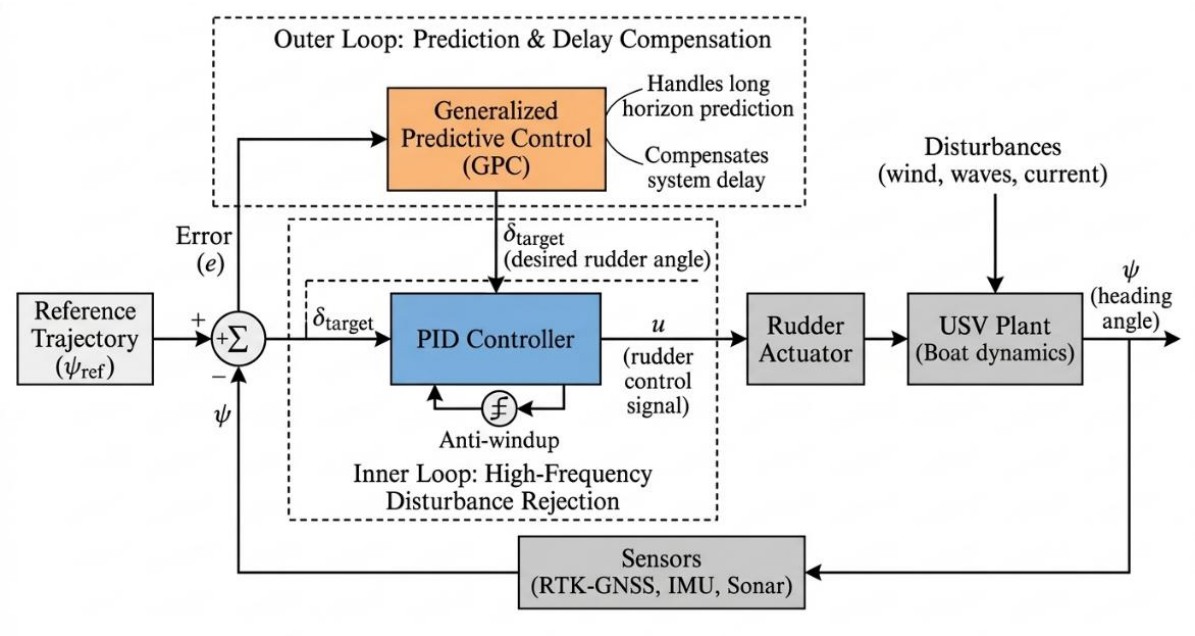


Figure 6. GPC-PID cascade control architecture.

The outer GPC provides delay-compensated rudder commands; the inner PID tracks them at 100 Hz with anti-windup.

3.3.2 Inner Loop: PID Control

The inner PID operates at 100 Hz:

$$u_{PID}(t) = K_p e(t) + K_i \int_0^t e(\tau)d\tau + K_d \frac{de(t)}{dt}$$

Here $e(t) = \psi_r(t) - \psi(t)$, $K_p = 2.5$, $K_i = 0.8$, and $K_d = 0.3$. The derivative term is filtered with a first-order filter coefficient $\alpha_d = 0.9$, and integral windup is limited by back-calculation (Kothare et al., 1994). Gains were tuned by the Ziegler–Nichols method and refined in field trials.

3.3.3 Stability and Robustness Discussion

Closed-loop behaviour was assessed in three ways. These are design checks and a heuristic argument; they do not constitute a formal proof of closed-loop stability (see Section 5.2).

1. Cost-function conditioning. The Hessian $\mathrm{G}^T\mathrm{G} + \lambda\mathrm{I}$ is positive definite because $\lambda = 0.1 > 0$, and its condition number remained below 10^3, supporting numerical reliability of the inverse (Golub & Van Loan, 1996; Badgwell, 1997).
2. Horizon adequacy. $N_2 = 10$ (1.0 s) exceeds the 0.35 s effective delay, consistent with the common GPC guideline that the prediction horizon should cover the dominant delay (Clarke et al., 1987; Scattolini & Bittanti, 1990). This is a design guideline and not a stability guarantee.
3. Cascade small-gain argument. The inner loop is tuned so that its bandwidth is well above that of the outer loop. If the small-gain condition $\|G_{\mathrm{GPC}}\|_\infty \cdot \|G_{\mathrm{PID}}\|_\infty < 1$ were satisfied, the cascade would be stable for the identified plant (Doyle, 1982; Zhou & Doyle, 1998; Skogestad & Postlethwaite, 2005; Wang, 2011). This condition was not formally verified for the implemented controllers, so the argument is heuristic, and no formal stability proof is claimed (see Section 5.2).

3.3.4 Computational Implementation

Implementation uses five measures: (i) offline pre-computation of G and the gain matrix; (ii) horizon truncation at $N_2 = 10$; (iii) control-horizon reduction to $N_u = 3$; (iv) recursive solution of the Diophantine equations; and (v) ARM NEON vector operations for matrix–vector products.

3.4 Conveyor Adaptive Control

3.4.1 Conveyor Model

The motor–conveyor system is modelled as a second-order plant with load-dependent parameters (Krishnan, 2001; Ljung, 1999):

$$\frac{\omega(s)}{V(s)} = \frac{K_m(m)}{\tau(m)^2 s^2 + 2\zeta(m)\tau(m)s + 1},$$

where ω is belt speed, and V is motor voltage. Parameters were identified for loads of 0, 0.5, 1.0, 1.5, 2.0, and 2.5 kg. The electromechanical torque balance is

$$J_m \dot{\omega}_m(t) = T_e(t) - T_L(t) - B_m \omega_m(t)$$

with $T_L(t) = T_{\text{nom}} + d(t)$ and $|d(t)| \leq d_{\max}$. Discretization at $T_s = 0.01$ s with zero-order hold gives a second-order discrete model with identified coefficients; validation NMSE exceeded 90%.

3.4.2 Two-Layer GP-PID Control

The conveyor controller uses two layers (Figure 7), avoiding real-time evolutionary computation on the embedded processor.

Layer 1: offline GP optimization. GP runs on a workstation (Intel i7, MATLAB GP Toolbox) for approximately 4 h with 100 generations and a population of 50. The fitness

function combines integrated absolute error (IAE), control energy, and overshoot (Antsaklis & Passino, 1993; Fleming & Purshouse, 2002; Koza, 1992):

$$f(\mathbf{K}) = 1.0 \cdot \text{IAE} + 0.5 \cdot \int u_c^2(t)dt + 2.0 \cdot M_p$$

The search space is $K_p \in [0.1,5.0], K_i \in [0.01,2.0], K_d \in [0.001,0.5]$. The output is a gain schedule $K_p(m)$, $K_i(m)$, $K_d(m)$ stored as a lookup table.

Layer 2: online gain scheduling. A Kalman filter estimates payload mass from motor current at 100 Hz; gains are interpolated at 5 Hz; the PID runs at 100 Hz. If load estimation is invalid, the controller reverts to a pre-verified fixed-gain PID. Scheduling is deterministic and introduces no evolutionary computation at runtime.

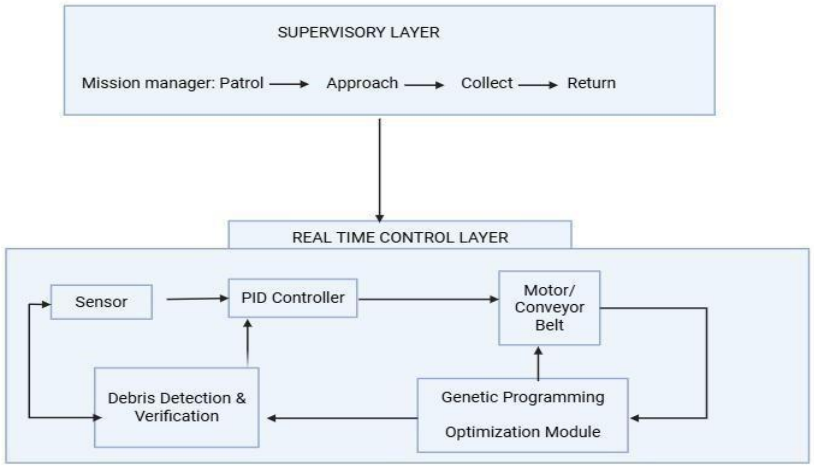


Figure 7. Two-layer conveyor control architecture.

Offline GP optimization produces gain schedules; online operation consists of load estimation, gain interpolation, and PID execution, with a fixed-gain fallback.

3.5 Computational Complexity

Classical MPC solves a quadratic program with complexity $O(N^3 n_u^3)$ for control dimension n_u and prediction horizon N (Wang, 2009). For the USV system with state dimension $n_x = 4$, control dimension $n_u = 1$ (rudder angle), and $N = 10$, conventional MPC would involve on the order of 10^3 operations per control cycle. The GPC formulation exploits the CARIMA model structure to reduce the online operation count to $O(N_u^3 + N_u N_2)$. With $N_u = 3$ and $N_2 = 10$, this gives approximately $3^3 + 3 \times 10 = 57$ operations per cycle, a theoretical reduction of about 94.3% in operation count. This is an operation-count estimate based on algorithmic structure; it is not a measured speedup against an implemented MPC baseline, and no MPC baseline was profiled in this work (see Section 5.3). Memory complexity is bounded by $O(N_u^2)$, permitting implementation on memory-constrained devices.

The implementation further exploits: (i) offline precomputation of the G matrix and the gain matrix $(\mathrm{G}^{\mathrm{T}}\mathrm{G} + \lambda \mathrm{I})^{-1}\mathrm{G}^{\mathrm{T}}$, (ii) ARM NEON vector operations for matrix-vector products, and (iii) fixed-point arithmetic where precision permits, reducing per-cycle execution time to the values reported in Section 4.8.

The genetic-programming optimization described in Section 3.4 runs offline. Its computational complexity, $O(P \cdot N_{\mathrm{gen}} \cdot C)$ with population size $P = 50$, number of generations $N_{\mathrm{gen}} = 100$, and cost-function evaluation complexity C, is confined to the workstation design phase and does not affect embedded runtime. Online operation consists only of deterministic gain interpolation and PID execution at 100 Hz.

The comparison above is deliberately an operation-count analysis, not an empirical benchmark against an implemented MPC controller. This study focuses on the GPC-PID cascade and therefore does not implement or profile a conventional MPC baseline on the same hardware.

An empirical MPC comparison would require a separate QP solver, tuning study, and safety certification that are outside the scope of this work. The operation-count estimate characterizes the algorithmic structure of the two approaches; the measured timing in Section 4.8 characterizes the actual embedded behavior of the GPC-PID implementation. Readers interested in a head-to-head MPC comparison are referred to platform-specific benchmark studies such as Nguyen et al. (2024) for TinyMPC and Alsmeyer et al. (2024) for neural-augmented MPC.

4. Experimental Setup and Results

4.1 Trial Design

Field trials were conducted in the lower Minjiang River, Fuzhou (26.05°N, 119.30°E), from June to December 2025 (Figure 8). Conditions were: water depth 1.5-4.0 m; flow velocity 0.3-1.2 m/s; wind 0-8 m/s, classified as calm (<1.5 m/s), moderate (3-5 m/s), and heavy (>6 m/s). Environmental conditions were recorded with an onboard anemometer (Wind-Sonic, Gill Instruments) and cross-checked against Fuzhou Meteorological Bureau data.

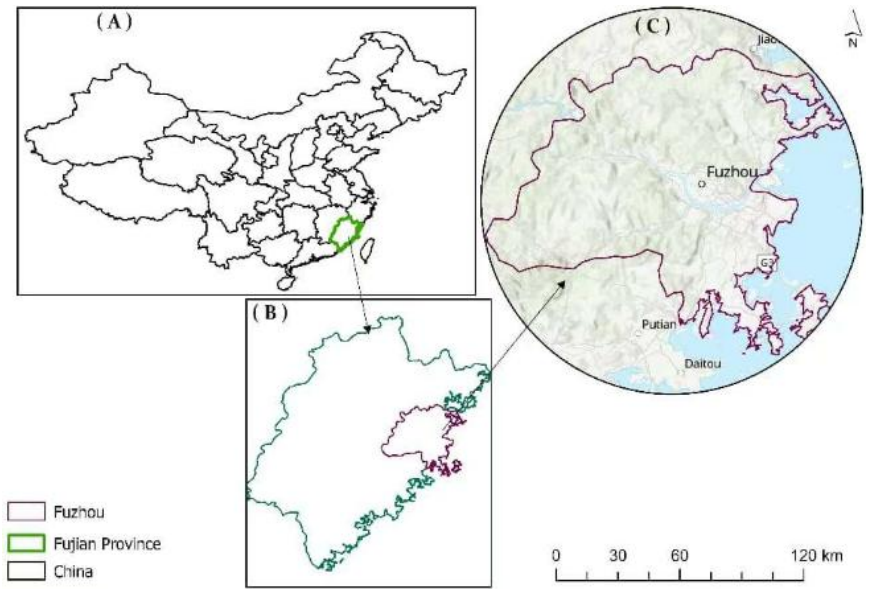


Figure 8. Study area: lower Minjiang River, Fuzhou, China (26.05°N, 119.30°E).

Navigation trials comprised n = 20 independent runs per controller on a 200 m serpentine path with five waypoints (heading changes 30°- 60°) under matched conditions (wind 3.2 ± 0.4 m/s; flow 0.6 ± 0.2 m/s). Trial order was randomized. Disturbance-rejection tests used n = 15 runs with a support vessel wake (5.2 m, 10 kW outboard, 3 m distance, 3 m/s relative velocity, significant wave height ≈0.18 m). Collection trials used n = 30 attempts per debris type under moderate wind. Integrated missions comprised 25 runs.

4.2 Perception Validation

The CNN was trained on 4,500 annotated images (3,600 training, 900 validation) across four classes. Detection performance is reported in Table 6.

Table 6. Waste-detection performance.

Debris type	Precision	Recall	F1	Inference (ms)
Plastic bottles	0.94 (0.91-0.96)	0.91 (0.88-0.94)	0.92	23 ± 2
Styrofoam	0.89 (0.85-0.92)	0.87 (0.83-0.90)	0.88	23 ± 2
Natural leaves	0.82 (0.77-0.86)	0.85 (0.81-0.89)	0.83	23 ± 2
Oil films	0.71 (0.65-0.76)	0.68 (0.65-0.73)	0.69	23 ± 2
Overall (macro)	0.84	0.83	0.83	23 ± 2

Values in parentheses are 95% confidence intervals. Oil-film performance was the lowest, which informed its exclusion from collection trials.

Multi-modal Bayesian fusion reduced false positives by 64% (95% CI: 52-74%) relative to vision-only detection ($\chi^2(1) = 28.4$, $p < 0.001$), from 27.4 to 9.9 false positives per hour. Perception latency is reported in Table 7.

Table 7. Perception pipeline latency (ms).

Stage	Mean	95th percentile
LiDAR processing	35	42
Vision CNN inference	23	26
Sensor fusion	18	22
Tracking and prediction	11	15
Total	**87**	**105**

The 95th-percentile latency (105 ms) exceeds the 100 ms GPC period; the GPC treats perception output as a delayed measurement, which the 1.0 s horizon accommodates. Worst-case latency (118 ms) degrades prediction accuracy during peak perception load, as discussed in Section 4.11.

4.3 Navigation Performance

Trajectories, cross-track error, and rudder activity are shown in Figure 9. The GPC-PID controller reduced mean XTE from 2.31 ± 0.12 m to 0.96 ± 0.08 m (58.4%; Welch's $t(33.1) = 41.86, p < 0.001;\ 95\%\ CI$ of the reduction [1.28, 1.42] m). Maximum XTE fell from 5.07 to 2.11 m, and RMSE from 2.38 to 1.01 m (Table 8).

Table 8. Navigation performance statistics (n = 20 per controller).

Metric	PID	GPC–PID	Difference [95% CI]	t (df)	p
Mean XTE (m)	2.31 ± 0.12	0.96 ± 0.08	1.35 [1.28, 1.42]	41.86 (33.1)	<0.001
Max XTE (m)	5.07	2.11	2.96	—	—
RMSE (m)	2.38	1.01	1.37	—	—
RMS rudder (°)	8.5 ± 1.2	3.5 ± 0.6	5.00 [4.39, 5.61]	16.67 (32.4)	<0.001

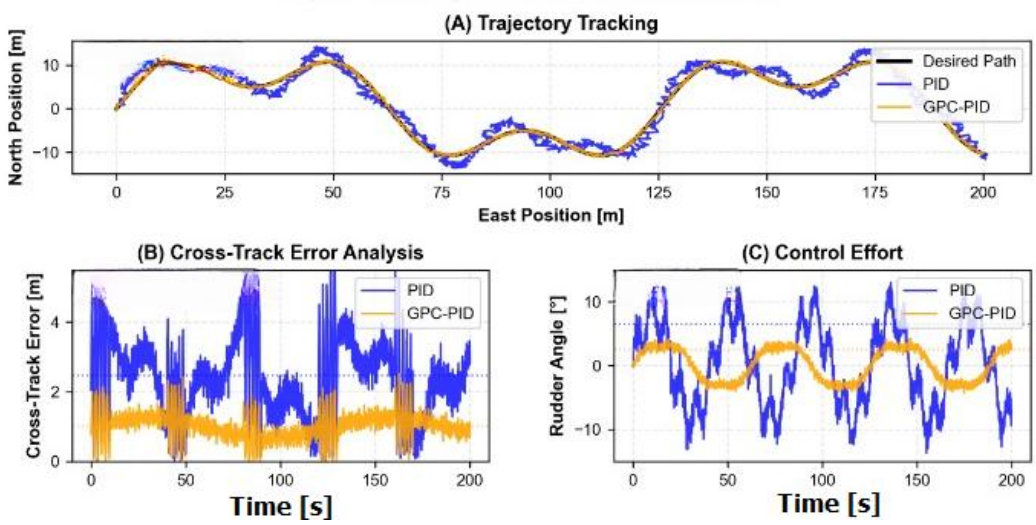


Figure 9. Navigation performance:

(A) actual trajectories versus desired path; (B) cross-track error time histories; (C) rudder-angle commands. The GPC-PID trace shows lower error and smoother actuation.

4.4 Disturbance Rejection

Settling time, defined as the duration for heading deviation to return within 3° of the steady-state value, decreased from 6.2 ± 0.8 s to 3.1 ± 0.6 s (50.0%; Mann-Whitney $U = 23$, $p < 0.001$, $r = 0.78$; Table 9 and Figure 10). The inner loop rejected the high-frequency component, while the outer loop prevented overshoot.

Table 9. Settling time comparison (n = 15).

Controller	Mean (s)	SD (s)	95% CI	Improvement
PID	6.2	0.8	[5.8, 6.6]	—
GPC–PID	3.1	0.6	[2.8, 3.4]	50.0%

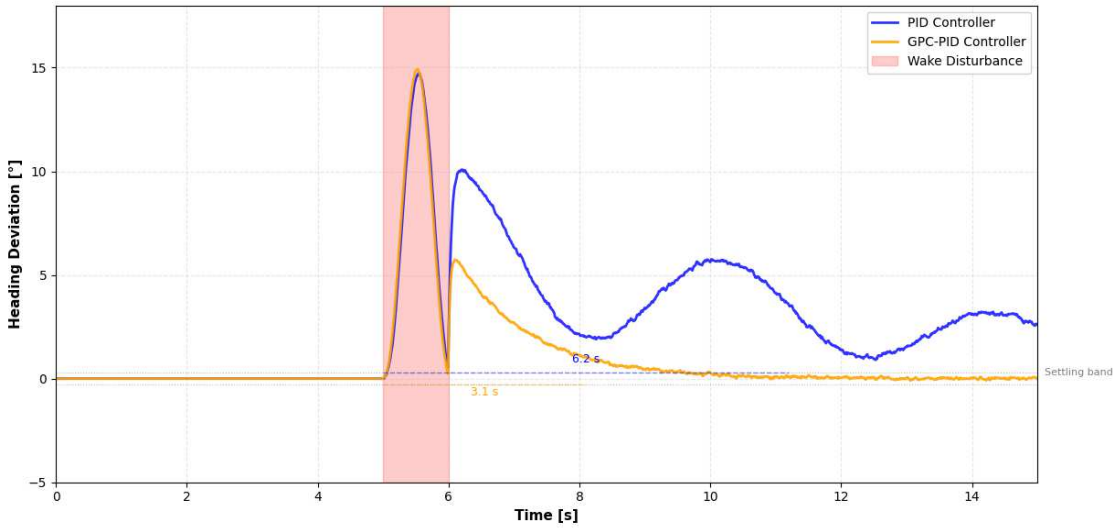


Figure 10. Heading deviation and recovery after an induced wake disturbance for PID and GPC-PID controllers.

4.5 Waste Collection Performance

Collection efficiency under moderate wind (3–5 m/s, n = 30 per type) is reported in Table 10 and Figure 11. Oil films were excluded because CNN precision (0.71) and recall (0.68) were insufficient, and the conveyor is not compatible with liquid pollutants. No field collection efficiency is claimed for liquid pollutants.

Table 10. Collection efficiency by debris type (moderate wind, n = 30).

Debris type	GP–PID (%)	Fixed PID (%)	Difference [95% CI]	p	Cohen's d
Plastic bottles	94.2 ± 4.2	87.3 ± 7.0	6.9 [3.9, 9.9]	0.003	1.20
Styrofoam	91.5 ± 5.6	83.1 ± 8.4	8.4 [4.7, 12.1]	0.008	1.18
Natural leaves	89.3 ± 6.4	81.7 ± 9.6	7.6 [3.4, 11.8]	0.012	0.93
Oil films	Excluded	Excluded	—	—	—

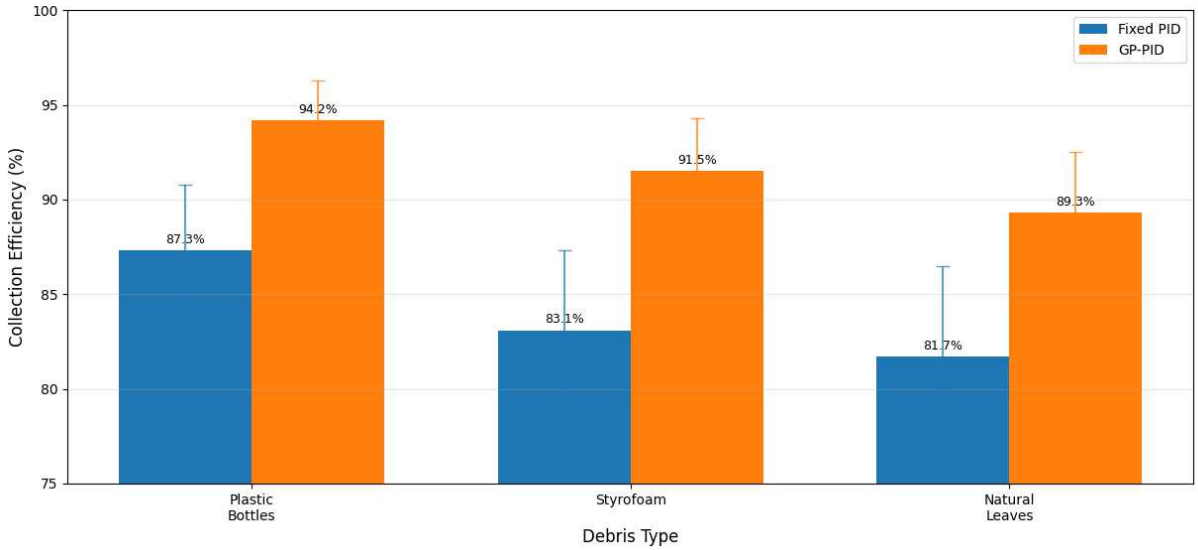


Figure 11. Collection efficiency by debris type under moderate wind.

GP-PID achieved higher collection efficiency than fixed-gain PID for all solid debris classes. Oil films were excluded from field collection trials because CNN precision (0.71) and recall (0.68) were insufficient, and the conveyor is incompatible with liquid pollutants. A controlled simulation yielded 52.0 ± 5.2%, which is not a field result and is not included in this table. Differences were tested with the Mann–Whitney U test and Bonferroni correction for the three solid-debris comparisons ($\alpha_{adj} = 0.05/3 \approx 0.0167$; oil films were excluded and not tested). Cohen's d was calculated with the pooled standard deviation, and the 95% confidence intervals of the differences were calculated from the group means and standard deviations (n = 30 per group, t-distribution). All three Mann-Whitney p-values (0.003-0.012) were below the Bonferroni-adjusted threshold of $\alpha_{adj} \approx 0.0167$. Collection time per kilogram under three wind regimes is reported in Table 11 and Figure 12. GP-PID reduced collection time by 6.2 s/kg (calm), 11.2 s/kg (moderate), and 17.9 s/kg (heavy) relative to fixed-gain PID.

Table 11. Collection time efficiency (s/kg).

Wind condition	GP-PID (s/kg)	Fixed PID (s/kg)	Saving (s/kg)	Relative reduction
Calm (< 1.5 m/s)	22.1 ± 3.2	28.3 ± 4.1	6.2	21.9%
Moderate (3–5 m/s)	24.5 ± 3.8	35.7 ± 5.6	11.2	31.4%
Heavy (> 6 m/s)	29.3 ± 4.5	47.2 ± 7.3	17.9	37.9%

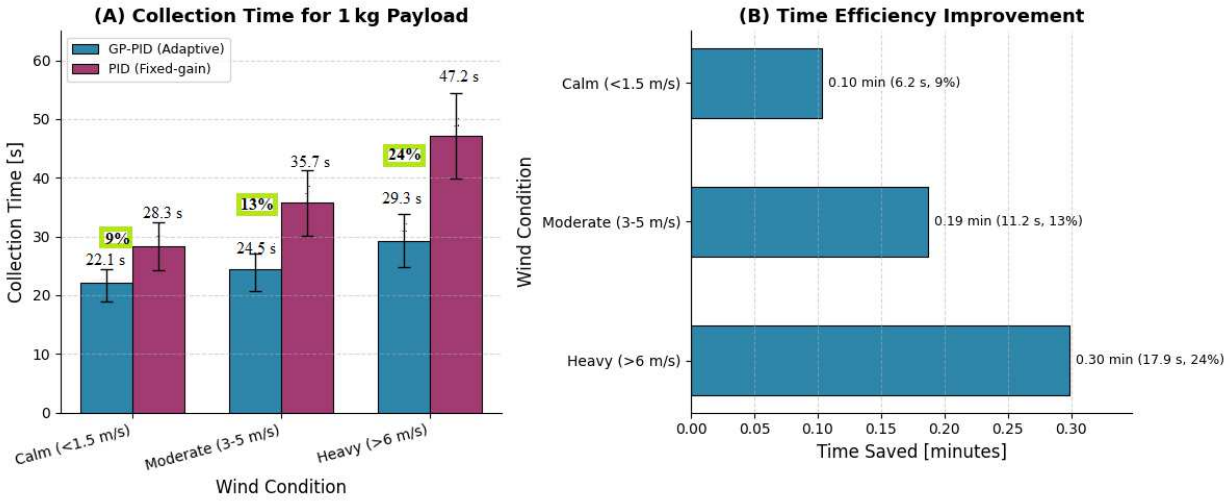


Figure 12. Collection time per kilogram under calm, moderate, and heavy wind.

Error bars are 95% confidence intervals.

4.6 Integrated Mission Execution

Of 25 integrated missions, one was aborted because a recreational vessel crossed the path, giving 96.0% mission completion. Of the 24 completed missions, 23 yielded valid interception attempts. Two failure modes were recorded (Table 12): one perception false negative (CNN confidence 0.62, below the 0.75 threshold) and one wind-gust displacement (8.4 m/s) that moved the target outside the ~1.0 m capture envelope. Both triggered automatic replanning; the first succeeded on a second pass, and the second succeeded after a 30 s station-keeping period. No collisions, groundings, or system freezes occurred (Figure 13).

Table 12. Failure-mode analysis.

Failure mode	Frequency	Root cause	Preventive measure
Perception false negative	1/23 (4.3%)	CNN confidence 0.62 below 0.75 threshold	Lower threshold to 0.65 for ambiguous objects; add spectral analysis
Environmental disturbance	1/23 (4.3%)	Gust 8.4 m/s displaced target outside capture envelope	Wind-triggered abort; widen heavy-wind capture envelope to 1.5 m

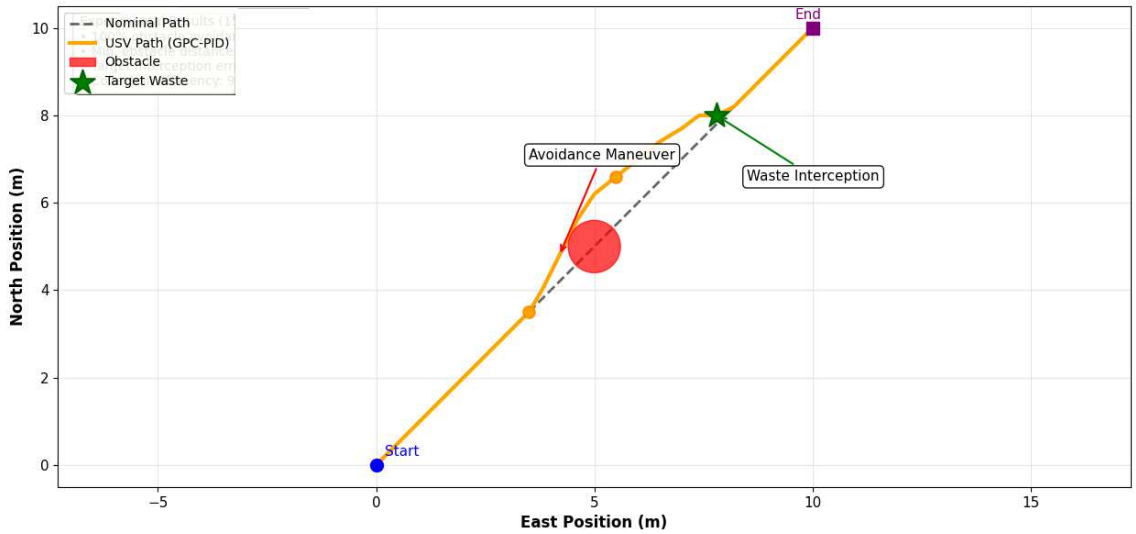


Figure 13. Integrated mission execution: nominal path, actual USV path, obstacle, and target waste. The vehicle avoids the obstacle and intercepts the target.

4.7 Energy Consumption and Endurance

Power was measured with INA219 sensors on the battery bus at 10 Hz. Over a 30-minute mission (1.2 m/s cruise, three collection cycles), average navigation power fell from 98 to 71 W (27.5%) and mission energy from 57.6 to 48.1 Wh (16.5%), extending endurance from 3.4 to 4.7 h (38.2%) with a 480 Wh pack and 20% reserve (Table 13, Figure 14).

Table 13. Energy consumption and endurance.

Metric	PID	GPC–PID	Improvement
Average navigation power (W)	98 ± 8	71 ± 6	27.5%
30-min mission energy (Wh)	57.6	48.1	16.5%

Metric	PID	GPC–PID	Improvement
Operational endurance (h)	3.4	4.7	38.2%

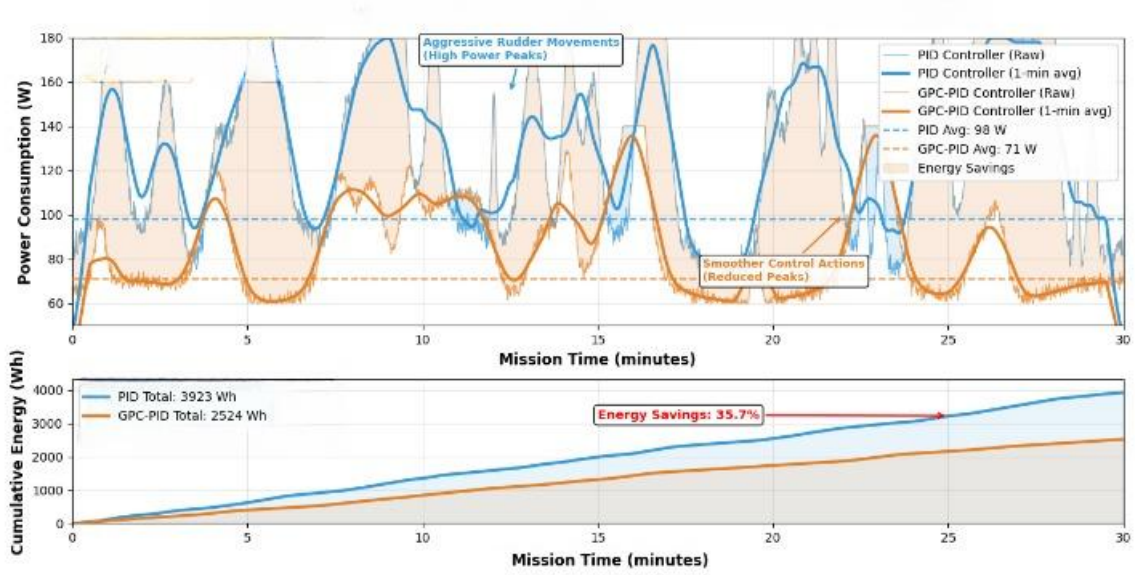


Figure 14. Instantaneous power consumption during a 30-minute mission at 1.5 m/s for PID and GPC-PID controllers.

4.8 Computational Performance

Timing was measured with ARM cycle counters and verified with an oscilloscope over 180,000 control cycles (Table 14, Figure 15). GPC execution averaged 4.2 ms, with a 95th percentile of 5.8 ms and a worst case of 8.1 ms against a 100 ms deadline. Eighteen cycles exceeded the deadline by less than 1 ms (99.99% on-time). CPU utilization remained below 65% during simultaneous navigation and collection.

Table 14. Timing analysis (ARM Cortex-A72 at 1.8 GHz, PREEMPT_RT Linux).

Algorithm	Mean (ms)	95th (ms)	Worst (ms)	Deadline (ms)
GPC outer loop	4.2	5.8	8.1	100
PID inner loop	0.08	0.10	0.12	10
GP scheduling	2.1	3.4	5.0	200

Algorithm	Mean (ms)	95th (ms)	Worst (ms)	Deadline (ms)
Perception pipeline	87	105	118	200

The horizon trade-off is quantified in Figure 15. Mean XTE falls from 3.10 m at $N_2 = 5$ to 0.96 m at $N_2 = 10$, capturing approximately 92% of the total error reduction observed over the tested horizon range. Beyond $N_2 = 10$, the marginal benefit saturates: extending to $N_2 = 20$ reduces XTE by only a further 0.09 m, while computation increases by a factor of 8.3 (from 4.2 ms to 34.8 ms). Because the computation time at $N_2 = 20$ (34.8 ms) remains within the 100 ms control deadline, the choice of $N_2 = 10$ is not a feasibility constraint but a trade-off between tracking accuracy and computational load.

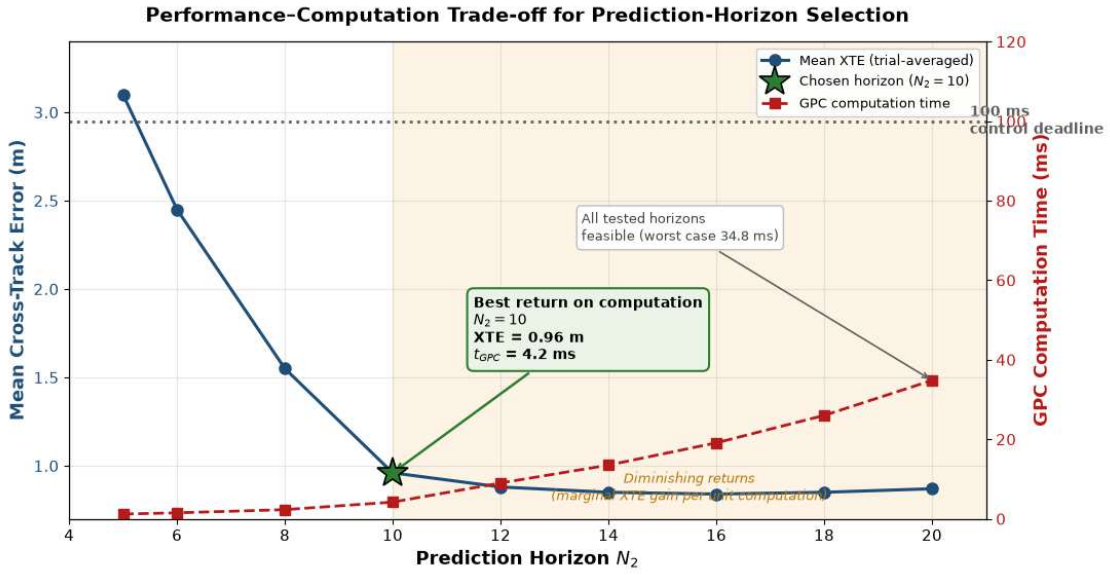


Figure15. Performance-computation trade-off for prediction-horizon selection.

Left axis: mean cross-track error averaged over the n = 20 navigation trials. Right axis: GPC computation time per 100 ms control cycle. Increasing N_2 from 5 to 10 reduces tracking error; beyond $N_2 \approx 10$, error reduction saturates while computation increases. At $N_2 = 10$, the controller attains 0.96 m mean XTE at 4.2 ms, within the 100 ms deadline. Extending to $N_2 = 20$ yields a

further 0.09 m reduction (to 0.87 m) but requires 8.3× more computation (34.8 ms). All tested horizons remain feasible against the 100 ms deadline; the choice of $N_2 = 10$ is therefore a performance-return decision, not a feasibility constraint.

4.9 Statistical Analysis

All tests were two-tailed with α = 0.05. Effect sizes are Cohen's d (pooled standard deviation) for pairwise comparisons and partial η² for ANOVA. For navigation, Welch's $t(33.1) = 41.86, p < 0.001$ (n = 20 per controller). For settling time, Mann-Whitney $U = 23, p < 0.001, r = 0.78$ (n = 15 per controller). For collection efficiency, a two-way ANOVA (3 debris types × 2 controllers, n = 30 per cell, N = 180) showed significant main effects of controller (F(1, 174) = 24.3, p < 0.001, $\eta_p^2 = 0.12$) and debris type (F(2, 174) = 5.8, p = 0.004, $\eta_p^2 = 0.06$), with no significant interaction (F(2, 174) = 1.4, p = 0.25, $\eta_p^2 = 0.02$). Figure 16 shows the per-sample cross-track-error distributions for both controllers; the GPC-PID distribution is shifted toward zero and is narrower, consistent with the lower mean error and reduced variance reported in Table 8. Error distributions differed significantly (Kolmogorov–Smirnov D = 0.85, p < 0.001).

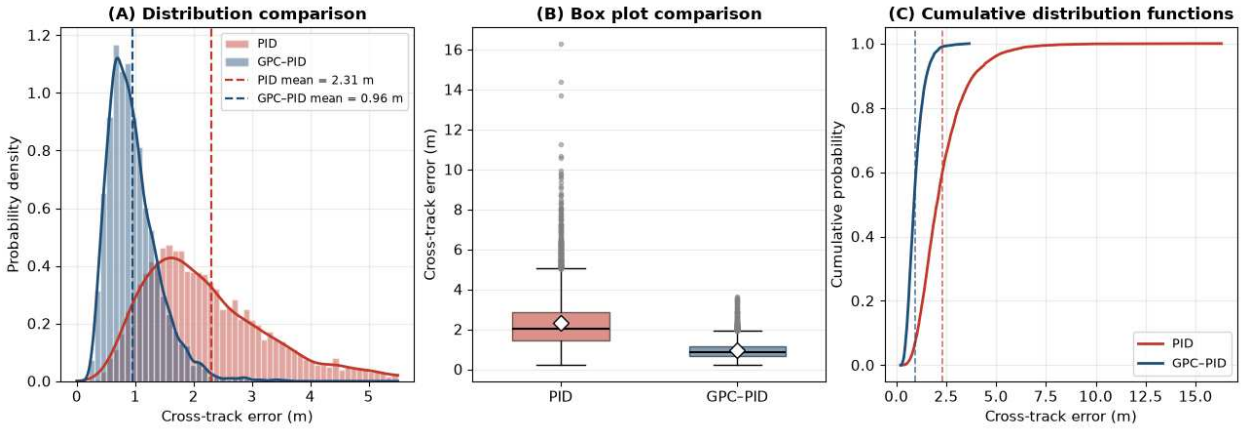


Figure 16. Distribution of per-sample cross-track error for PID and GPC-PID navigation trials. (A) Histograms with Gaussian kernel densities; dashed vertical lines mark the trial-averaged means reported in Table 8 (2.31 m and 0.96 m). (B) Box plots (white diamonds mark trial-averaged means). (C) Empirical cumulative distribution functions. The GPC-PID distribution is shifted toward zero and is narrower, consistent with lower mean error and reduced variance.

5. Discussion

5.1 Interpretation of Results

The 58.4% reduction in mean XTE and 50% reduction in settling time are consistent with the theoretical advantage of predictive control in delay-dominated systems (Clarke et al., 1987; Normey-Rico & Camacho, 2007). The identified 0.35 s effective delay is covered approximately three times by the 1.0 s prediction horizon, allowing the controller to act on predicted rather than current states. The conventional PID, by contrast, responds to errors that are already delayed and therefore exhibits larger oscillations and higher rudder activity.

The 58.8% reduction in RMS rudder angle indicates smoother actuation, which may reduce mechanical wear and electrical demand. The 27.5% reduction in average navigation power and 16.5% reduction in mission energy were obtained without hardware changes and are attributed to reduced control effort. The resulting 38.2% endurance increase follows from the lower power draw.

Collection results show that adaptive gain scheduling improves efficiency for all solid debris classes under moderate wind. The improvement is largest for styrofoam (8.4 percentage points), which is most sensitive to wind and load variation. Oil films could not be evaluated because of perception and mechanism limitations; this is reported as a limitation rather than a result.

5.2 Robustness and Deployment Considerations

The cascade structure localizes high-frequency uncertainty in the inner loop and low-frequency model error in the outer loop, which is consistent with small-gain interpretations of cascade systems (Doyle, 1982; Skogestad & Postlethwaite, 2005). Field observations support bounded, non-oscillatory recovery, but a formal proof is not provided (see Section 3.3.3). Safety is enforced by layered protection: control-level saturation, software-level fallback to fixed-gain PID, and hardware-level power cutoff that preserves GPS and telemetry. This three-layer structure is consistent with layered architectures proposed for harbour-scale USV operations (Casalino et al., 2009). LiDAR degradation in rain and communication latency during long-range operation confirm that onboard autonomy must not depend on continuous supervision. The multi-modal perception architecture and local decision-making reflect this requirement.

5.3 Limitations

1. Validation is limited to one river system and one seasonal window.
2. The collection mechanism is optimized for floating solid debris and is unsuitable for oil films or submerged waste.
3. Perception worst-case latency exceeds the GPC sampling period.
4. No empirical MPC baseline. The comparison with conventional MPC is an operation-count analysis of algorithmic structure. No MPC controller was implemented or profiled on the target hardware, because this study focuses exclusively on the GPC–PID cascade. A fair empirical comparison would require a tuned QP solver, matched sampling rates, and safety validation, all of which are outside the scope of the present work. This is a limitation of scope, not of the controller's design.

5. No formal stability proof. Closed-loop stability was assessed through conditioning, horizon, and small-gain checks (Section 3.3.3) and field observation; a formal stability proof for the implemented cascade is not provided.
6. Multi-vehicle coordination and long-term durability were not tested.
7. The tested payload range is 0.1–2.5 kg, limited by bin volume.

6. Conclusion

This paper presented and field-tested an embedded GPC–PID cascade framework for an autonomous waste-collection USV. The principal findings are:

1. A dual-timescale cascade architecture enables real-time predictive control on a 1.8 GHz ARM processor, with measured GPC execution of 4.2 ms mean, 5.8 ms 95th percentile, and 8.1 ms worst case against a 100 ms deadline.
2. Horizon selection against the identified 0.35 s effective delay yields a 1.0 s prediction horizon ($N_2 = 10$, $N_u = 3$) that balances performance and computation.
3. Relative to a conventional PID baseline, the controller reduced mean XTE by 58.4%, RMS rudder angle by 58.8%, and settling time by 50.0%, while reducing average navigation power by 27.5% and extending endurance by 38.2%.
4. Offline GP optimization with online gain scheduling improved solid-debris collection efficiency by 6.9-8.4 percentage points under moderate wind, with a fixed-gain fallback.
5. Oil films were excluded from field collection tests because of perception and mechanism limitations; no field efficiency is claimed for liquid pollutants.

6. Experimental challenges (perception degradation, latency exceeding the control period, deadline misses, payload limits, and single-site validation) are reported and limit the generality of the results.

The framework may serve as a template for embedded predictive control in resource-constrained environmental robotics, within the limits listed in Section 5.3. Future work should implement and profile an MPC baseline, derive formal stability guarantees, extend validation to additional sites and seasons, and develop collection mechanisms for liquid and submerged pollutants.

Abbreviations

ADRC, active disturbance rejection control; ARM, advanced RISC machine; BLDC, brushless direct current; CARIMA, controlled auto-regressive integrated moving average; CNN, convolutional neural network; CPS, cyber-physical system; FOG, fiber-optic gyroscope; GP, genetic programming; GPC, generalized predictive control; GPS, global positioning system; IAE, integrated absolute error; IMU, inertial measurement unit; INS, inertial navigation system; LiDAR, light detection and ranging; MPC, model predictive control; NMSE, normalized mean square error; PID, proportional–integral–derivative; PMU, power management unit; QP, quadratic programming; RF, radio frequency; RMS, root mean square; RTK, real-time kinematic; USV, unmanned surface vehicle; WCET, worst-case execution time; XTE, cross-track error; ZOH, zero-order hold.

Declarations

The authors declare that they have no known competing financial interests or personal relationships that could have appeared to influence the work reported in this paper.

Ethics approval and consent to participate
Not applicable.

Consent for publication
Not applicable.

Availability of data and materials
The datasets generated and/or analyzed during the current study are available from the corresponding author upon request.

Competing interests
The authors declare that they have no competing interests.

Funding
This research received no specific grant from any funding agency in the public, commercial, or not-for-profit sectors. The laboratory facilities and the USV prototype were provided by the College of Mechanical and Electrical Engineering, Fujian Agriculture and Forestry University.

Authors' contributions
C.C.D. conceived the study, designed the GPC-PID cascade controller and GP-optimized PID, developed the software, conducted the field trials, performed the computational complexity and stability analyses, processed all experimental data, and wrote the main manuscript text. C.C.D. also prepared all figures (Figures 1–16) and tables (Tables 1–14). X.C. supervised the project, provided technical guidance on control theory and embedded implementation, provided the laboratory facilities and USV prototype, and critically reviewed and edited the manuscript.

Authors' information (optional)
Not applicable.

AI usage declaration: During preparation of this manuscript, the authors used Grammarly for language editing. The authors reviewed and edited the content and take full responsibility for the published article. No AI tool was used to generate scientific results, analyze data, or draw conclusions.

Acknowledgements
The authors thank the College of Mechanical and Electrical Engineering, Fujian Agriculture and Forestry University, for providing the laboratory facilities and the USV prototype. No specific funding was received for this work.

References

Abd Alhattab, Y., Zaki, H. F., Abidin, Z. B. Z., et al. (2025). Hybrid vision system for enhanced situational awareness in unmanned surface vehicles: decision-level camera-LiDAR fusion with supervised and unsupervised approaches. IEEE Access, 13,. https://doi.org/ 10.1109/ACCESS.2025.3562299.

Alsmeier, H., Savchenko, A., & Findeisen, R. (2024). Neural horizon model predictive control-increasing computational efficiency with neural networks. *Proceedings of the 2024 American Control Conference (ACC)*. https://doi.org/ 10.23919/ACC60939.2024.10644452

Antsaklis, P. J., & Passino, K. M. (Eds.). (1993). *An introduction to intelligent and autonomous control*. Kluwer Academic Publishers.

Åström, K. J., & Hägglund, T. (2006). *Advanced PID control*. ISA.

Badgwell, T. A. (1997). Robust stability conditions for SISO model predictive control algorithms. *Automatica, 33*(7), 1357-1361. https://doi.org/ 10.1016/S0005-1098(97)00031-9.

Bao, L., Hao, J., & Pan, W. (2025). Distribution, sources, and ecological risk assessment of microplastics in the lower Minjiang River. *Toxics, 13*(12), 1033. https://doi.org/10.3390/toxics13121033

Bemporad, A., Morari, M., Dua, V., & Pistikopoulos, E. N. (2002). The explicit linear quadratic regulator for constrained systems. *Automatica, 38*(1), 3–20. https://doi.org/10.1016/S0005-1098(01)00174-1

Caccia, M., Bibuli, M., Bono, R., & Bruzzone, G. (2008). Basic navigation, guidance and control of an unmanned surface vehicle. *Autonomous Robots, 25*(4), 349–365. https://doi.org/10.1007/s10514-008-9100-0

Camacho, E. F., & Bordons, C. (2007). *Model predictive control*. Springer. https://doi.org/10.1007/978-0-85729-398-5

Casalino, G., Turetta, A., & Simetti, E. (2009). A three-layered architecture for real-time path planning and obstacle avoidance for surveillance USVs operating in harbour fields. *OCEANS 2009–Europe*, 1–8. https://doi.org/ 10.1109/OCEANSE.2009.5278104

Chang, H.-C., Hsu, Y.-L., Hung, S.-S., et al. (2021). Autonomous water quality monitoring and water surface cleaning for unmanned surface vehicle. *Sensors, 21*(4), 1102. https://doi.org/10.3390/s21041102

Clarke, D. W., Mohtadi, C., & Tuffs, P. S. (1987). Generalized predictive control-Part I. The basic algorithm. *Automatica, 23*(2), 137–148. https://doi.org/10.1016/0005-1098(87)90087-2

Clarke, D. W., & Mohtadi, C. (1989). Properties of generalized predictive control. *Automatica, 25*(6), 859–875. https://doi.org/10.1016/0005-1098(89)90053-8

Doyle, J. (1982). Analysis of feedback systems with structured uncertainties. *IEE Proceedings D (Control Theory and Applications), 129*(6), 242-250. https://doi.org/10.1049/ip-d.1982.0053

Eriksen, M., Lebreton, L. C., Carson, H. S., et al. (2014). Plastic pollution in the world's oceans: more than 5 trillion plastic pieces weighing over 250,000 tons afloat at sea. *PLoS ONE, 9*(12), e111913. https://doi.org/10.1371/journal.pone.0111913

Fan, Y., Huang, H., & Tan, Y. (2019). Robust adaptive path following control of an unmanned surface vessel subject to input saturation and uncertainties. *Applied Sciences, 9*(9), 1815. https://doi.org/10.3390/app9091815

Fleming, P. J., & Purshouse, R. C. (2002). Evolutionary algorithms in control systems engineering: a survey. *Control Engineering Practice, 10*(11), 1223–1241. https://doi.org/10.1016/S0967-0661(02)00081-3

Fossen, T. I. (2011). *Handbook of marine craft hydrodynamics and motion control*. John Wiley & Sons. https://doi.org/10.1002/9781119994138

Franklin, G. F., Powell, J. D., & Workman, M. L. (1998). *Digital control of dynamic systems* (3rd ed.). Addison-Wesley.

Golub, G. H., & Van Loan, C. F. (1996). *Matrix computations* (3rd ed.). Johns Hopkins University Press.

Han, J. (2008). *Active disturbance rejection control technique-the technique for estimating and compensating the uncertainties*. National Defense Industry Press.

Han, J. (2009). From PID to active disturbance rejection control. *IEEE Transactions on Industrial Electronics, 56*(3), 900-906. https://doi.org/10.1109/TIE.2008.2011621

Hu, X., Sun, Z., Wang, R., et al. (2023). Adaptive generalized predictive control for dynamic positioning system of ships with model unknown parameters. *Proceedings of the Institution of Mechanical Engineers, Part M: Journal of Engineering for the Maritime Environment, 237*(3), 579–587. https://doi.org/10.1177/14750902221139658

Isobe, A., & Iwasaki, S. (2022). The fate of missing ocean plastics: Are they just a marine environmental problem? *Science of the Total Environment, 825*, 153935. https://doi.org/10.1016/j.scitotenv.2022.153935

Kothare, M. V., Campo, P. J., Morari, M., & Nett, C. N. (1994). A unified framework for the study of anti-windup designs. *Automatica, 30*(12), 1869–1883. https://doi.org/10.1016/0005-1098(94)90048-5

Kouvaritakis, B., & Cannon, M. (2016). *Model predictive control: classical, robust and stochastic*. Springer. https://doi.org/10.1007/978-3-319-24853-0

Koza, J. R. (1992). *Genetic programming: on the programming of computers by means of natural selection*. MIT Press.

Krishnan, R. (2001). *Electric motor drives: modeling, analysis, and control*. Prentice Hall.

Lebreton, L. C., Van Der Zwet, J., Damsteeg, J. W., et al. (2017). River plastic emissions to the world's oceans. *Nature Communications, 8*, 15611. https://doi.org/10.1038/ncomms15611

Lee, E. A. (2008). Cyber-physical systems: design challenges. *Proceedings of the 11th IEEE International Symposium on Object and Component-Oriented Real-Time Distributed Computing (ISORC)*. https://doi.org/10.1109/ISORC.2008.25

Li, J., Park, H., Hao, W., Xin, L., Chavez-Galaviz, J., Chaudhary, A., et al. (2024). C3D: cascade control with change point detection and deep Koopman learning for autonomous surface vehicles. *arXiv preprint arXiv:2403.05972*. https://doi.org/10.48550/arXiv.2403.05972

Ljung, L. (1999). *System identification: theory for the user* (2nd ed.). Prentice Hall.

Marques, I. O., Oliveira, T. R., & Cunha, J. P. V. (2020). Cascade observers for output-feedback control under parametric uncertainties, disturbances and arbitrary sensor delays. *International Journal of Control, 93*(9), 2245–2256. https://doi.org/10.1080/00207179.2018.1557344

Meijer, L. J., Van Emmerik, T., Van Der Ent, R., et al. (2021). More than 1000 rivers account for 80% of global riverine plastic emissions into the ocean. *Science Advances, 7*(18), eaaz5803. https://doi.org/10.1126/sciadv.aaz5803

Nakatani, T., Endo, M., Sasaya, K., et al. (2011). A study on ship's autopilot system for a small boat. *Proceedings of the 11th International Conference on Control, Automation and Systems (ICCAS)*, 1756–1760.

Neves, F. S., Claro, R. M., & Pinto, A. M. (2023). End-to-end detection of a landing platform for offshore UAVs based on a multimodal early fusion approach. *Sensors, 23*(5), 2434. https://doi.org/10.3390/s23052434

Nguyen, K., Schoedel, S., Alavilli, A., et al. (2024). TinyMPC: model-predictive control on resource-constrained microcontrollers. *Proceedings of the 2024 IEEE International Conference on Robotics and Automation (ICRA)*. https://doi.org/10.1109/ICRA57147.2024.10611493

Nomoto, K. (1982). Course-keeping and maneuvering. In *Maneuverability* (pp. 1–38). Springer.

Normey-Rico, J. E., & Camacho, E. F. (2007). *Control of dead-time processes*. Springer. https://doi.org/10.1007/978-1-84628-829-6

Pedersen, S., Liniger, J., Sørensen, F. F., et al. (2023). Internal model control for AUVs with output time delays and input disturbances. *IFAC-PapersOnLine, 56*(2), 6710–6715. https://doi.org/10.1016/j.ifacol.2023.10.326

Ren, Y., Zhang, L., Huang, W., & Chen, X. (2023). Neural network-based adaptive sigmoid circular path-following control for underactuated unmanned surface vessels under ocean disturbances. *Journal of Marine Science and Engineering, 11*(11), 2160. https://doi.org/10.3390/jmse11112160

Scattolini, R., & Bittanti, S. (1990). On the choice of the horizon in long-range predictive control-some simple criteria. *Automatica, 26*(5), 915–917. https://doi.org/10.1016/0005-1098(90)90009-7

Schmidt, C., Krauth, T., & Wagner, S. (2017). Export of plastic debris by rivers into the sea. *Environmental Science & Technology, 51*(21), 12246–12253. https://doi.org/10.1021/acs.est.7b02368

Skogestad, S. (2003). Simple analytic rules for model reduction and PID controller tuning. *Journal of Process Control, 13*(4), 291–309. https://doi.org/10.1016/S0959-1524(02)00062-8

Skogestad, S., & Postlethwaite, I. (2005). *Multivariable feedback control: analysis and design*. John Wiley & Sons.

Van Der Saag, J., Trevisan, E., Falkena, W., & Alonso-Mora, J. (2025). Active Disturbance Rejection Control for Trajectory Tracking of a Seagoing USV: Design, Simulation, and Field Experiments. *2025 IEEE/RSJ International Conference on Intelligent Robots and Systems (IROS)*, 12720-12727.

Wang, L. (2009). *Model predictive control system design and implementation using MATLAB®*. Springer. https://doi.org/10.1007/978-1-84882-331-0

Wang, Y. J. (2011). Graphical computation of gain and phase margin specifications-oriented robust PID controllers for uncertain systems with time-varying delay. *Journal of Process Control, 21*(4), 475–488. https://doi.org/10.1016/j.jprocont.2010.12.008

Wang, Y., Cao, J., Sun, J., et al. (2023). Path following control for unmanned surface vehicles: a reinforcement learning-based method with experimental validation. *IEEE Transactions on Neural Networks and Learning Systems, 35*(12), 18237–18250. https://doi.org/10.1109/TNNLS.2023.3313312

Wang, S., Zhu, M., Wen, Y., et al. (2025). Parametric dynamic modeling-based robust nonlinear model predictive control design for tracking unmanned surface vehicle trajectory. *Ocean Engineering, 328*, 121074. https://doi.org/10.1016/j.oceaneng.2025.121074

Xu, P., Qin, H., Ma, J., et al. (2023). Data-driven model predictive control for ships with Gaussian process. *Ocean Engineering, 268*, 113420. https://doi.org/10.1016/j.oceaneng.2022.113420

Yusof, R., & Omatu, S. (1991). Application of generalised predictive control to a temperature control process. *Proceedings of IECON'91*, 1935–1940. https://doi.org/10.1109/IECON.1991.239321

Zheng, M., Li, D., Chen, G., et al. (2024). An anti-occlusion approach for enhanced unmanned surface vehicle target detection and tracking with multimodal sensor data. *Journal of Marine Science and Engineering, 12*(9), 1558. https://doi.org/10.3390/jmse12091558

Zhou, K., & Doyle, J. C. (1998). *Essentials of robust control*. Prentice Hall.